

REVIEW

Open Access

State-of-health estimation of lithium-ion batteries based on electrochemical impedance spectroscopy: a review

Yanshuo Liu¹, Licheng Wang^{2*}, Dezhi Li¹ and Kai Wang^{1*} 

Abstract

Lithium-ion batteries (LIBs) are crucial for the large-scale utilization of clean energy. However, because of the complexity and real-time nature of internal reactions, the mechanism of capacity decline in LIBs is still unclear. This has become a bottleneck restricting their promotion and application. Electrochemical impedance spectroscopy (EIS) contains rich electrochemical connotations and significant application prospects, and has attracted widespread attention and research on efficient energy storage systems. Compared to traditional voltage and current data, the state-of-health (SOH) estimation model based on EIS has higher accuracy. This paper categorizes EIS measurement methods based on different principles, introduces the relationship between LIBs aging mechanism and SOH, and compares the advantages of different SOH estimation methods. After a detailed analysis of the latest technologies, a review is given. The insights of this review can deepen the understanding of the relationship between EIS and the aging effect mechanism of LIBs, and promote the development of new energy storage devices and evaluation methods.

Keywords Lithium-ion batteries, State-of-health, Electrochemical impedance spectroscopy, SOH estimation, Battery management system

1 Introduction

Lithium-ion batteries (LIBs) stand out among batteries because of their high energy density, being environmentally protective, and having no memory effect. They have become the most promising energy storage component in the twenty-first century, and are widely used in many fields such as electric vehicles and aerospace [1–4]. The LIB industry has entered a critical stage of industrialization of construction and application. In the next few years, with the development of downstream demand-side

industries, the demand for LIBs will continue to have a high growth rate [5–10].

The electrode material of LIBs is one of the key factors restricting their development, and therefore it has been a research focus in recent years [11, 12]. As well as the electrode material of LIBs, the state of health (SOH) is also an important parameter [2]. It is well known that battery management systems (BMS) can assess the SOH of batteries, provide risk warnings, and ensure the long-term safe and stable operation of batteries. Among them, accurate battery state estimation is the key to BMS, and the study of SOH is helpful in grasping the influencing factors of battery aging [13]. Knowing the current battery SOH is helpful in judging the inherent danger and life of LIBs, and in providing a reference for the maintenance and replacement of the battery. In addition, the accurate estimation of SOH is also very important for the economic evaluation of batteries. The estimation of LIBs' SOH is also essential for the expansion of the recycling

*Correspondence:
Licheng Wang
wanglicheng@zjut.edu.cn

Kai Wang
wkwj888@163.com
¹ School of Electrical Engineering, Weihai Innovation Research Institute, Qingdao University, Qingdao 266000, China
² School of Information Engineering, Zhejiang University of Technology, Hangzhou 310014, China

industry to determine whether batteries will be recycled as scrap metal or used in “Second Life” applications with lower requirements [13–19]. As shown in Fig. 1, retired LIBs can still be reused. For both new and echelon utilization batteries, accurate SOH estimation will help to estimate the overall life of LIBs, improve the charging and discharging strategies and avoid battery abuse.

A typical BMS collects current–voltage response curve data in the time domain. Therefore the features derived from the charging and discharging curves are by far the most commonly used inputs [21–26]. Compared with the usual current/voltage data, electrochemical impedance spectroscopy (EIS) has been proposed as a fast, non-invasive and reliable technique, which has been widely used to characterize and simulate the behavior of LIBs [27, 28]. During the testing process, a wide frequency range is applied to reflect the impedance spectrum information (real part, imaginary part, phase) of the battery at different temperatures and State of Charge (SOC). The use of EIS can fully reflect the changes in the cathode, anode, electrolyte, solid electrolyte layer, and other aspects of LIBs during the aging process. Compared with traditional BMS and non-destructive testing techniques, it has the advantages of fast detection speed and rich reflection information [29].

Currently, the methods of estimating battery SOH using EIS are mainly divided into model-based and data-driven methods [30]. The method based on the model is to fit the EIS measured at different temperatures and SOC states to the built model. The parameters of the equivalent circuit and the reconstructed discharge curve can be obtained, so as to study their cycle performance and to know if they have been abnormally aging during operation. Physical effects occurring in any electrochemical system can be associated with the electrical parameters of the ECM, which helps quantify the phenomena

that occur within LIBs during charging, discharging and aging. Unlike model-based methods, data-driven methods do not need to take into account the electrochemical mechanisms of LIBs, but learn potential characteristics from a large amount of historical information to predict future sequence trends [31, 32].

EIS can also be used in power battery models, and its parameter changes are related to the electrochemical reactions inside the LIBs [33, 34]. EIS is highly practical, and research has proved that there is an inherent relationship between battery impedance and SOH [35–37]. This method can not only better understand the actual degradation process of the battery over a wide frequency range, but also be used to estimate the life characteristics of the battery. However, because of the disadvantages of more complicated measurements, and the need for high precision and special measuring instruments, impedance devices on small electronic equipment are limited by cost, power consumption and equipment complexity. With the gradual development of electronic technology, chip-level impedance measurement technology is gradually maturing, which provides a new direction for SOH estimation [38–41].

The rest of this paper is arranged as follows. Section 2 introduces the principles and measurement methods of the impedance spectrum, while Sect. 3 describes the relationship between the aging mechanism with LIBs and EIS. Section 4 summarizes the existing SOH estimation methods from two aspects, and finally, in Sect. 5, the existing SOH estimation methods based on EIS are summarized.

2 Principle and measurement of electrochemical impedance spectroscopy

2.1 Electrochemical impedance spectroscopy (EIS)

EIS, also known as AC impedance spectroscopy, is a non-destructive method for characterizing LIBs. The basic principle of an electrochemical impedance spectrum is to perturb the electrochemical steady-state system with a sinusoidal excitation signal of small amplitude and frequency f . The change of the ratio of the excitation voltage and the response current is the impedance spectrum of the electrochemical system [42, 43]. Since the amplitude change is very small, the positive and negative phases cancel each other. Therefore, it has a very weak influence on the battery, and is a nondestructive measurement method close to steady state. By analyzing the frequency, amplitude and phase relationship between the excitation signal and the response signal, the frequency response function of the tested system over a certain frequency range can be obtained. In constant current mode, the sinusoidal current ΔI is superimposed onto the DC current I of the lithium battery [35]:

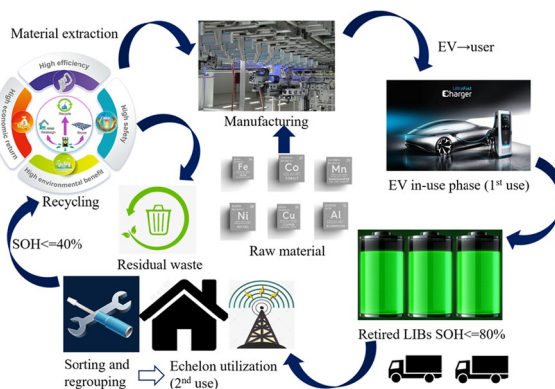


Fig. 1 Disposal route for echelon utilization of retired power LIBs.
Reprinted with permission from [20]. Copyright 2022, MDPI

$$\Delta I = I_{\max} \sin(2\pi ft) \quad (1)$$

The voltage response of the excitation signal can be measured as:

$$\Delta V = V_{\max} \sin(2\pi ft + \phi) \quad (2)$$

where the amplitude of the voltage response V_{\max} and the phase ϕ are determined at the particular frequency. In potentiostatic mode, the opposite occurs i.e. where a sinusoidal voltage is superimposed onto the battery DC voltage (V) [35]. Likewise, the amplitude of the current response I_{\max} and the phase ϕ are determined at the frequency. The impedance for both galvanostatic and potentiostatic methods is defined by [35]:

$$Z(f) = \frac{V_{\max}}{I_{\max}} e^{j\phi} \quad (3)$$

Equation (3) can be simplified using the Euler formula, $e^{j\phi} = \cos(\phi) + j\sin(\phi)$, as:

$$\begin{aligned} Z(f) &= \frac{V_m}{I_m} e^{j\phi} = \frac{V_m}{I_m} [\cos(\phi) + j\sin(\phi)] \\ &= Z_0[\cos(\phi) + j\sin(\phi)] \\ &= Z_0 \cos(\phi) + Z_0 \sin(\phi)j \end{aligned} \quad (4)$$

As shown in Fig. 2, an impedance spectrum is formed as different perturbation frequencies make different responses. Reference [44] proposes a graphical analysis of impedance data in Bode and Nyquist representations:

- (1) The "Nyquist plot" describes the relationship between the real and imaginary parts of the impedance. Different regions correspond to various chemical and physical processes occurring in the battery, and it is usually used to analyze the characteristics of LIBs in combination with ECM.
- (2) The "Bode plot" shows the phase shifts and magnitude changes, which play an important role in the

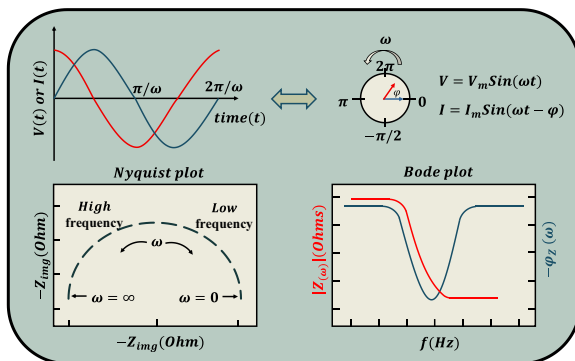


Fig. 2 EIS measurement principle, Nyquist and Bode diagrams

research on sensors, filters and transistors in electronic devices [33].

Since the Nyquist plot is convenient for analyzing the mechanism of an active reaction, it is more commonly used in analyzing the characteristics of LIBs [45].

2.2 Measurement of electrochemical impedance spectroscopy

2.2.1 Frequency domain measurement

The frequency domain measurement principle of EIS is to select the frequency range of the excitation signals and determine different frequency points, and then use the excitation signals of different frequency points for sweep measurement. The amplitude and phase of the excitation and response signals of the same frequency are analyzed to obtain the frequency response characteristics of the system and finally the EIS [46]. Most of the measuring instruments used in research are commercial electrochemical workstations of a three-electrode structure. However, the existence of wire resistance, parasitic capacitance and parasitic inductance on the connectors may cause measurement errors. Because commercial electrochemical workstations widely use the frequency sweeping method, only one frequency point can be measured at a time. This leads to slow measurement speed. If the measurement time is too long, the state of the battery may change, resulting in inaccurate EIS results. Therefore this method is usually used for offline research in the laboratory. In addition, because of the complexity and high cost of the equipment, its application is limited and it is difficult to implement in engineering.

2.2.2 Time domain measurement of impedance spectrum

In order to obtain the EIS of LIBs quickly, researchers have proposed some computation methods using time-domain signal processing technology [44]. The transient signal is applied to the battery in the time domain, and then the input and response signals are mathematically converted to the frequency domain. EIS is obtained by the quotient of response signal and input signal spectra. In [47], a step signal is applied to the ECM and the response is converted into the frequency domain through Laplace transform to obtain the model impedance, whereas [48] applies mixed sinusoidal current signals with the same amplitude, different frequencies and phases to LIBs, to obtain EIS through Fourier transform (FT). Reference [49] proposes a measurement method based on the Fast Fourier transformation (FFT), which realizes fast measurement of the impedance spectrum. Through this method, the measurement

time can be reduced by 2/3 and its accuracy is almost the same as those of existing instruments. In [50], a method is put forward for diagnosing battery impedance based on transient response using continuous wavelet transform, while [51] uses a pseudo-random binary sequence as an interference signal and successfully estimates the battery cell impedance using Morlet continuous wavelet transform. The EIS time-domain measurement method is easy to implement and apply, but there are still some challenges in practical applications. For example, because of the influence of state variables such as temperature, the sensitivity of battery impedance measurement will be very high. Therefore, it is necessary to balance between measurement time and measurement precision, and further optimize the existing measurement methods.

2.2.3 Inspection of impedance data

Effective EIS measurement requires that the measured spectrum meet three conditions of causality, linearity and stability [52]:

- (a) Causality condition: the output response signal can only be caused by the input disturbance signal.
- (b) Linear condition: the current and potential of the electrochemical system are nonlinear relations determined by the dynamics law. When a small amplitude sine wave potential signal is used to disturb the system, the relationship between the potential and current can be approximately regarded as linear. The amplitude of the potential sine wave as a disturbance signal is typically about 5 mV, and generally does not exceed 10 mV.
- (c) Stability condition: the disturbance will not cause the internal structure of the system to change. When the disturbance stops, the system can return to the original state.

In order to check whether the measured EIS meets the requirements, there are currently mainly two methods. The first is to verify them through experiment. However, most of these methods require in-depth understanding of the excitation and response signals during impedance measurement, while most common frequency response analyzers cannot provide these signals. The second principle is based on analyzing the impedance spectrum obtained using Kramers–Kronig (K-K) relations [53]. By comparing the predicted Z_{imag} from data Z_{real} with the actual Z_{imag} , the residual ΔZ_{imag} is obtained. Analysis of K-K residuals reveals distortions in both the real and imaginary components

of acquired EIS data at high ($> 25 \text{ kHz}$) [54] and low frequencies [55].

3 Relationship between aging of LIBs and EIS

3.1 The aging mechanism of LIBs

Degradation in LIBs is caused by a large number of physical and chemical mechanisms that affect the different components of the battery, including electrodes, electrolytes, separators, and collectors [28, 56–59]. Figure 3 shows the degradation mechanism of LIBs. Because there are many factors affecting the aging of LIBs with dependencies between them, most physics-based models only focus on the important mechanisms, such as the formation and growth of solid electrolyte interface (SEI) films [60, 61].

Most degradation mechanisms of LIBs do not correspond to only one region on the impedance curve, and the same region may be affected by multiple degradation mechanisms [27, 62–64]. It is worth noting that the same degradation mechanism will also have different effects in different types of LIBs. In [27], the change in EIS is classified in more detail. This divides the corrosion of the collector into high frequency regions, lithium electroplating and SEI layer processes (growth and decomposition) into the mid-frequency region, and cathode particle cracking to the low frequency region. The relationship between aging of a lithium-ion battery and impedance curve is shown in Table 1.

High frequency region: it is the intersection of the impedance curve and the X axis. This is the total resistance of the electrolyte, active material, collector and separator. It is mainly composed of the resistance of electrolyte, but is also affected by the resistance between electrode metal, electrode lead, terminal and contact point. The growth of the SEI layer and the decomposition of electrolyte are the main degradation mechanisms affecting change in the high frequency region [68, 75]. In [65], the thickness of the SEI layer is measured, and the increase of ohmic resistance is found to be attributed to the growth of the SEI layer. Reference [67] attributes the

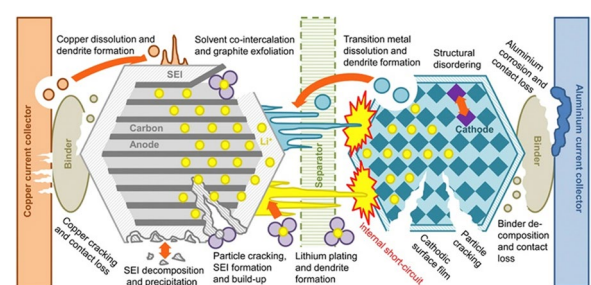


Fig. 3 Degradation mechanisms in LIBs. Reprinted with permission from [62]. Copyright 2017, Elsevier B.V.

Table 1 Correlation between impedance curve change and degradation mechanism

EIS region	Degradation mechanism					
	SEI growth	Li plating/dendrites formation	Electrolyte decomposition	CEI formation and charge transfer slow down	Corrosion of current collectors	Particle cracking of the cathode
Ohmic region	[65]	[66]	[66–68]		[67]	
Mid-frequency region [semarch 1]	[69–73]					
Mid-frequency region [semarch 2]				[71–73]		
Low-frequency region						[74]

increase in ohmic resistance to the corrosion of current collectors and the decomposition of electrolytes, and a similar conclusion is proposed in [66]. They show that electrolyte decomposition and SEI layer growth caused by the formation of thin films on the surface of lithium electroplating can lead to an increase in ohmic resistance. In addition, the growth of the SEI layer also affects the intermediate frequency region of the impedance curve.

Mid-frequency region (1st semicircle): The first semicircle in the intermediate frequency region of the impedance curve is related to the SEI layer formed by electrolyte decomposition on the anode surface [72]. This reaction forms a layer of SEI layer containing lithium on the electrode surface, and the formation of the SEI layer makes the electrolyte unable to reach the electrode surface, thus hindering the insertion of lithium. Therefore, SEI growth can lead to the loss of recyclable lithium, which reduces the battery capacity. The impedance spectrum of an aged battery (LCO) is studied at 100% DOD in [69], and it is observed that the impedance in the intermediate frequency region increases significantly, which is attributed to the growth of the SEI layer. In [70], the growth of SEI layer is assigned to the first arc of the impedance curve.

Mid-frequency region (2nd semicircle): The second semicircle in the intermediate frequency region represents the double-layer capacitance (C_{dl}) and charge transfer resistance (R_{ct}) existing at the interface between the battery electrode and the electrolyte. When ions are adsorbed to the electrode surface, a double-layer effect occurs at this interface, which consists of two parallel and opposite charge layers surrounding the electrode. Reference [73] uses the three-electrode configuration to study the impedance change of NCA batteries. An increase in impedance is observed in the intermediate frequency region, the change of the first half arch is attributed to the growth of the SEI layer, and the change of the second half arch is attributed to the slowing down of cathode charge transfer. In [71], the effect of high-rate discharge on NCA battery aging is studied, and the experimental results show that the impedance increases in the middle frequency region: the growth and structural damage to the cathode SEI layer are less because of the first half

arch, and the decomposition of the cathode SEI layer and the formation of CEI are due to the second half arch. Similarly, in [72], the impedance rise in the ohmic region and the first half arch of the intermediate frequency are assigned to SEI layer growth, while the impedance rise in the second part of the intermediate frequency region is assigned to CEI formation.

Low-frequency region: It is used to describe the diffusion phenomenon in the low-frequency region. The diffusion phenomenon describes the movement (quality transmission) of charged and uncharged particles to balance the concentration difference caused by the change of electrochemical potential. In addition, the concentration difference is mainly affected by the structural changes in the active substances [74].

3.2 Fitting equivalent circuit model

Although the electrochemical model can describe the electrochemical reaction inside the battery more accurately, it is too complicated to be estimated in real-time [76]. Commonly used ECMs are mainly divided into two categories: (a) Integer order model (IOM); and (b) Fractional order model (FOM). A lot of recent research has used FOM to model LIBs [77]. It can accurately estimate the dynamic behavior of LIBs using fewer computational resources [78]. Since ordinary capacitors are not sufficient to simulate the dynamic characteristics of real batteries at intermediate frequency, a constant phase element (CPE) is introduced to describe film capacitors that consider the dispersion effect. CPE has no direct physical significance, and it is used to describe the dispersion effect and its behavior deviating from capacitance. When its exponent is equal to 1, it behaves as a capacitor, and when its exponent is equal to 0, it behaves as a resistor.

The expression of ECM is a strong nonlinear equation about impedance measurement frequency, and the selection of initial parameters is very important to solve the nonlinear equation [44]. When the initial parameter selection is not appropriate, the impedance spectrum fitting will not converge, resulting in incorrect parameters. Fitting the ECM can be performed by complex nonlinear least squares (CNLS) [27, 73, 79]. Real and imaginary

components are fit simultaneously with uniform weighting, and the objective function to minimize is [80]:

$$X^2 = \sum_{n=0}^N [Z_{data}'(\omega_n) - Z_{model}'(\omega_n)]^2 + [Z''_{data}(\omega_n) - Z''_{model}(\omega_n)]^2 \quad (5)$$

where N is the frequency number of the real and imaginary parts of the impedance, Z'_{data} and Z''_{data} are the real and imaginary parts of the real impedance data respectively, Z'_{model} and Z''_{model} are the corresponding real and imaginary parts of the impedance data after fitting.

In the ECM of LIBs, each area in the Nyquist diagram has corresponding circuit links. The fitted ECM is usually composed of a resistor (R), capacitor (C), inductor (L), CPE and Warburg (W) [81]. The Nyquist diagram of each component is shown in Fig. 4, where:

- (a) The ultra-high frequency (UHP) segment is a vertical line below the real axis, caused by the movement of electrons in the wire and the winding of the internal electrode [82], represented by the L . The intersection of the vertical line and the X axis represents the R formed by the movement of electrons in the solid metal and ions in the electrolyte phase.
- (b) The first arc in the middle frequency range is generated by lithium-ion diffusion through the SEI layer. RC elements are usually used for modeling in IOM, and the $ZARC$ element is used in the FOM. R_{SEI} represents SEI resistance.
- (c) The second arc in the middle frequency describes the charge transfer process in the electrode reaction. When ions are absorbed on the electrode surface, a double-layer effect occurs at the interface between the electrode and the electrolyte. The layers are separated by a layer of solvent molecules.

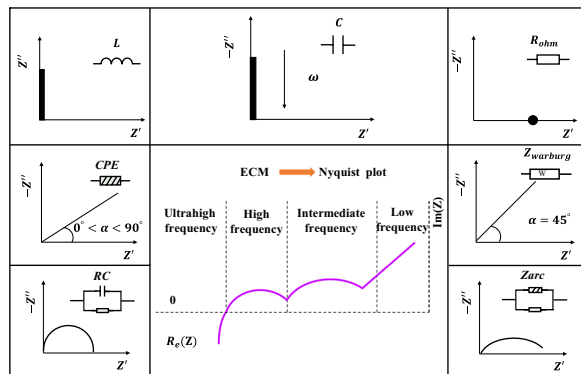


Fig. 4 Representation of ECM components on impedance spectrum curve

The behavior of the solvent layer is similar to that of the dielectric in a capacitor. Therefore, it is modeled as a capacitor [83]. The second constant phase element CPE is introduced to describe the double-layer capacitance, and R_{ct} represents the charge transfer resistance.

- (d) The low-frequency region: W is the Warburg impedance, i.e., the diffusion impedance of lithium ions in the electrode material. This usually presents as a straight line of approximately 45° on the Nyquist plot [84]. A phase shift of 0.5 can be observed on the Bode plot.

Figure 5 shows the more common ECMs. RC and $ZARC$ units are usually used to model the intermediate frequency region, which corresponds to the half arch of the intermediate frequency region [85]. The Warburg element is used to model the low-frequency region. The Warburg element is placed in series with other circuit elements or placed on the resistance branch of the second $RC/ZARC$ element to represent the diffusion tail. The ECM fitted by different research entry points will be slightly different. Increasing the number of networks can improve accuracy, but will sacrifice time and computing power [59, 86].

4 SOH estimation method based on EIS

4.1 Definition of SOH

The SOH of LIBs indicates the capacity of the current battery to store electric energy compared to the new battery, and represents the state of the battery from the beginning of its life to its end in the form of a percentage. The SOH of a new battery is 100%, and when the SOH of the battery reaches 80%, it is generally considered

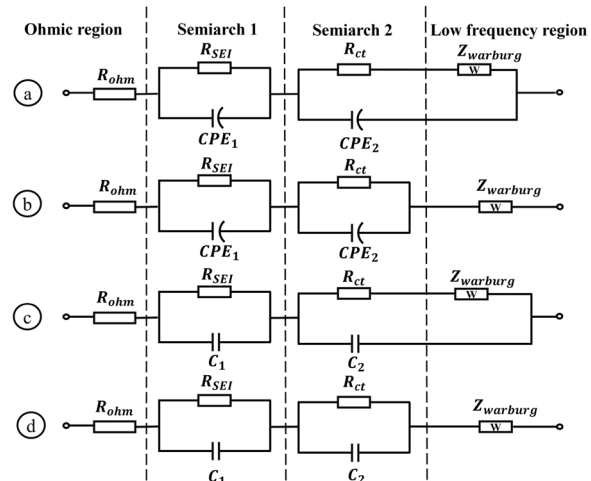


Fig. 5 Circuit diagram of common ECMs

that the end of the battery life has been reached [82]. SOH estimation is more challenging than state-of-charge (SOC) estimation [87]. As the battery cycles increase, the maximum available capacity decreases and the internal resistance increases. From the different performance characteristic parameters selected, two commonly used SOH definitions are given: one from the perspective of capacity, and the other from the perspective of internal resistance, shown as:

$$SOH = \frac{C_{now}}{C_0} \times 100\% \quad (6)$$

$$SOH = \frac{R_{EOL} - R_{now}}{R_{EOL} - R_{new}} \times 100\% \quad (7)$$

where C_{now} represents the maximum allowable discharge capacity, C_0 represents the nominal capacity of the battery, R_{now} represents the internal resistance at current time, R_{new} represents the internal resistance at current time from new cell, and R_{EOL} represents the internal resistance at the battery's end-of-life.

4.2 Method based on fitting equivalent circuit model

4.2.1 IOM

In the initial fitting model methods, most studies modeled LIBs through IOM models. In [81], the parameters of LIBs are characterized based on the traditional IOM model, but the relationship between the parameter changes and the SOH has not been studied. Reference [88] defines the SOH of batteries based on changes in ESR , R_{ct} and R_{sei} parameters in IOM. It is found that R_{sei} does not change significantly during discharge until 40% SOC, and then increases gradually after 30% SOC is exhausted. This demonstrates that R_{sei} changes more stably in different SOCs. The R_{ct} value has a concave behavior throughout the SOC scan. Subsequently, the resistance parameters are used as inputs to the artificial neural network for nonlinear fitting with the SOH. The error percentages for ESR , R_{sei} and R_{ct} are 5%, 1.5%, and 1%, respectively.

The main drawback of IOM is that it is impossible to match the low-frequency region of battery impedance in the frequency domain by using integer order ECM. However, CPE can well define low-frequency regions. In addition, a parallel combination of CPE and resistors is required to define the mid-frequency region of the EIS curve, which typically appears as a concave semicircle.

4.2.2 FOM

Compared with IOM, FOM can better characterize the characteristics of LIBs. Reference [89] proposes an FOM for a new generation LIBs electric vehicle model based on IOM, in which genetic algorithm-based model

Table 2 Defects of some methods based on ECM modeling

Reference	Part of impedance	Disadvantage
[92]	R_{SEI}	Temperature is not considered
[36, 93]	R_{ohm}	Temperature is not considered
[94]	R_{ct}	The relationship between R_{ct} and SOH is not quantitatively established

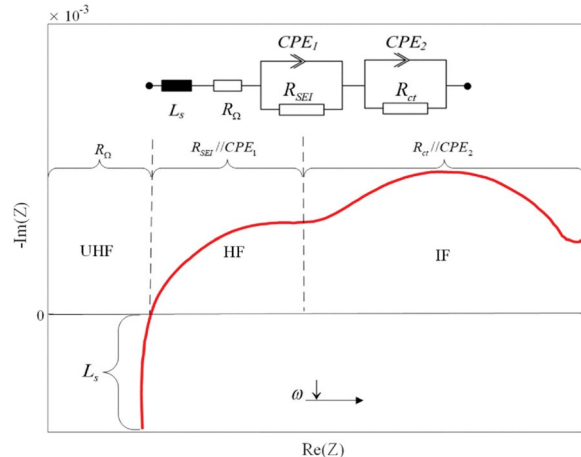


Fig. 6 FOM model. Reprinted with permission from [91]. Copyright 2021, IEEE

parameter identification and fractional order identification are also used. However, the effect of aging on battery models is not studied. In [90], the fitting algorithm for FOM parameters is introduced, based on the simplified main variables and a gradient-based optimization method. However, the battery model considered is too simple and the frequency range of the EIS spectrum studied is small (1 Hz–3 kHz).

Based on the aging mechanism of LIBs mentioned in Sect. 3, the corresponding FOM can be fitted through EIS data, and the SOH of batteries can be determined according to the regional variation. In [91], the shortcomings of relevant research (Table 2) are summarized and an FOM model is established as shown in Fig. 6. An exponential relationship between charge transfer resistance and residual capacity is proposed, and a probability model is established for the first time by combining environmental temperature and the SOC to achieve accurate estimation of LIBs in dynamic environments using the advantages of the ECM model and EIS measurement.

R_{ct} , which is affected by temperature and SOC, is selected as the impedance characteristic for estimating the SOH of LIBs. The SOH of batteries decays

exponentially with the charge transfer resistance, and their relationship is given as:

$$\begin{aligned} SOH(R_{ct}, T) &= \alpha \cdot \exp(x(T) \cdot R_{ct}) \\ &= \alpha \cdot \exp(\beta \cdot e^{\gamma * T} \cdot R_{ct}) \end{aligned} \quad (8)$$

where α , β , and γ are constant parameters, and $x(T)$ is the temperature function.

The above model is used to fit the battery data in different states of charge, given as:

$$SOH(R_{ct}, T, SOC) = \begin{cases} 1.026 \exp(-1.039R_{ct} \cdot e^{0.0729T}), SOC = 100\% \\ 1.058 \exp(-2.314R_{ct} \cdot e^{0.0717T}), SOC = 80\% \\ 1.049 \exp(-1.684R_{ct} \cdot e^{0.06462T}), SOC = 50\% \\ 1.037 \exp(-1.746R_{ct} \cdot e^{0.0739T}), SOC = 30\% \end{cases} \quad (9)$$

In addition, a probability model is constructed to map the relationship between the SOH and R_{ct} considering both temperature and the SOC, shown as:

$$SOH \sim N(\alpha \cdot \exp((\beta_1 \cdot SOC^2 + \beta_2 \cdot SOC + \beta_3) \cdot R_{ct} \cdot e^{\gamma * T}), \sigma) \quad (10)$$

where $\alpha, \beta_1, \beta_2, \beta_3, \gamma$ are parameters of the SOH mean, and σ is the uncertainty of the SOH.

In [95], a fractional impedance model is established through EIS data, and the discrete state space equation of the impedance model is derived according to the definition of Grunwald–Letnikov, which realizes the SOC estimation of LIBs. Similarly, reference [96] introduces a simplified fractional impedance model to characterize the performance of batteries (Fig. 7a). According to circuit theory and the equivalent circuit shown in Fig. 7a, the equation can be expressed as:

$$\begin{cases} V_0 = V_{OCV} + V_{ser} + V_1 + V_2 \\ V_{ser} = -R_{ser}I \\ -I = C_1 \Delta^\alpha V_1 + V_1/R_1 = C_2 \Delta^\beta V_2 + V_2/R_2 \\ \Delta^\alpha V_1 = -I/C_1 - V_1/R_1 C_1 \\ \Delta^\alpha V_2 = -I/C_2 - V_2/R_2 C_2 \end{cases} \quad (11)$$

where V_{ser} represents the voltage on the ohmic resistor (R_{ser}). The parallel combination of resistors and constant phase components is considered as $ZARC$. In addition, V_1 represents the voltage on $ZARC_1$, and can be used to characterize the concentration polarization phenomenon inside the battery. Finally, V_2 represents the active polarization voltage on $ZARC_2$.

FOM can be described as:

$$\begin{cases} \Delta^N x = Ax + BI \\ y = Cx + DI \end{cases} \quad (12)$$

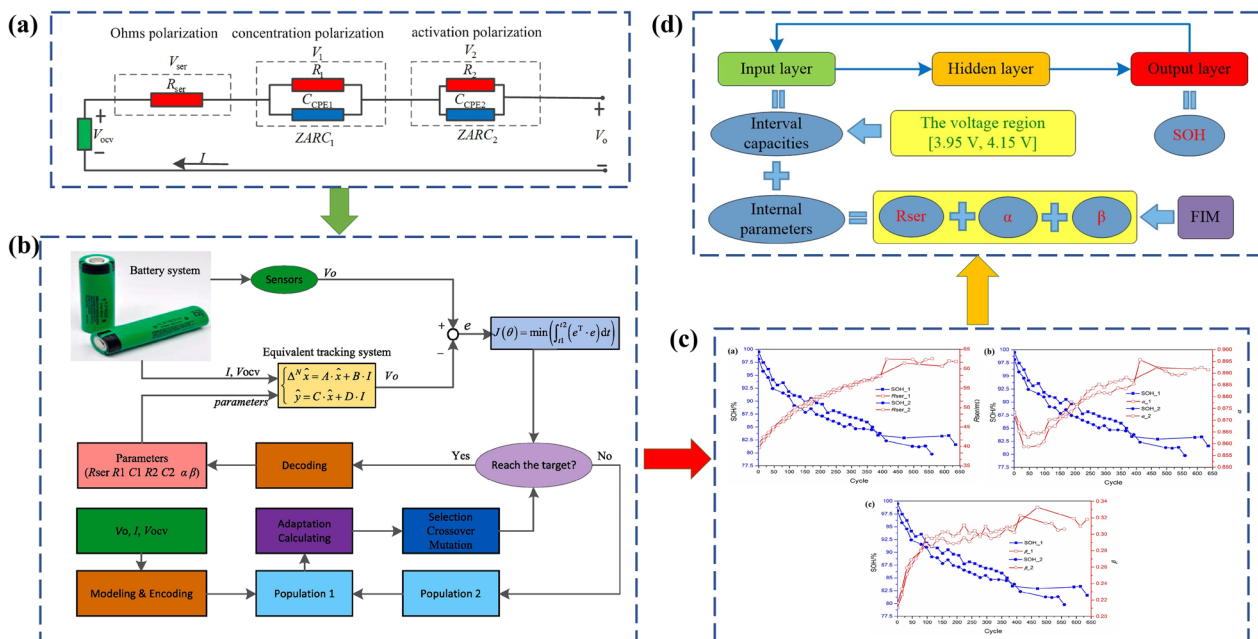


Fig. 7 Flow chart of SOH estimation based on FIM. **a** Simplified equivalent circuit based on the lithium-ion battery EIS and HPPC test. **b** Flow chart for parameter identification. **c** Internal parameter identification for batteries with different SOH. **d** SOH estimation based on BPNN. Reprinted with permission from [96]. Copyright 2020, Elsevier Ltd

where $A = \begin{bmatrix} -1/R_1C_1 & 0 \\ 0 & -1/R_2C_2 \end{bmatrix}$, $B = \begin{bmatrix} -1/C_1 \\ -1/C_2 \end{bmatrix}$, $C = [1, 1]$, $D = [-R_{ser}]$, $N = \begin{bmatrix} \alpha \\ \beta \end{bmatrix}$, $x = \begin{bmatrix} V_1 \\ V_2 \end{bmatrix}$, $y = [V_0 - V_{OCV}]$, and $x \in R^2$.

The Grünwald-Letnikov fractional order calculus is defined as:

$${}_a^G \Delta_t^r f(t) = \lim_{\substack{h \rightarrow 0 \\ kh=t-a}} h^{-r} \sum_{j=0}^k (-1)^j \binom{r}{j} f(t-jh) \quad (13)$$

where ${}_a^G \Delta_t^r$ is the fractional order calculus operator, h is the sampling period, k is the amount of sampling, and $\binom{r}{j}$ is the Newton binomial coefficient generalized to real numbers, which can be expressed as $\binom{r}{j} = \frac{r!}{j!(j-r)!}$.

This model combines fractional order theory and EIS information, and can fully balance the relationship between model complexity and computational efficiency. Identifying model parameters through a least squares genetic algorithm, the relationships between the SOH of the battery and the respective internal identification parameters, including Ohmic resistance (R_{ser}), polarization fractional order (α), and activation polarization fractional order (β), are shown in Fig. 7c. Because of the difficulties in accurately describing the relationships between battery SOH and these parameters using a function, a backpropagation algorithm is introduced to estimate the SOH based on the identified model parameters and interval capacity. The experimental results validate the effectiveness of this method, with an error margin of only $[-1.5\%, 1.5\%]$.

Reference [78] generates EIS data for a battery model using RLS technology (Fig. 8) combined with SVF based on FID parameters, and compares it with the actual EIS of lithium-ion batteries. The regression model obtained from the reconstructed EIS is then used in the particle filter (PF) framework to predict the RUL of the battery.

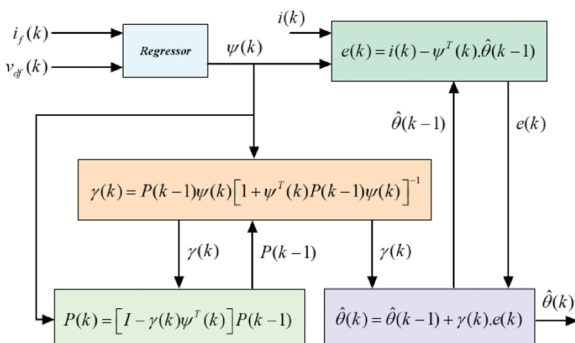


Fig. 8 Framework of the RLS method for online parameter estimation. Reprinted with permission from [78]. Copyright 2018, IEEE

This method can be implemented on an online platform without the need for measuring actual EIS data. In order to demonstrate the rationality of the proposed estimation method, comparative analysis is also conducted on IOM-based methods. Based on the observations of time domain, frequency domain, and life estimation behavior, it can be concluded that FOM exhibits better accuracy, with an R^2 value of 0.9978 and RMSE value of 0.0057.

4.3 Method based on data-driven

The data-driven approach does not rely on the aging mechanism of the battery, and can extract features related to battery SOH from a large amount of data, thus avoiding the complexity of model acquisition [97, 98]. With the development of deep learning, this method has received more attention and application.

4.3.1 Gaussian process regression

Gaussian Process Regression (GPR) has been used to estimate the SOH of LIBs in many studies [25, 99, 100]. GPR is a machine learning model based on Bayesian theory and kernel function. The model directly outputs the uncertainty (confidence interval) about the estimation point value and can give a better regularization effect without cross validation. The Gaussian process is composed of mean function $m(x)$ and covariance function $k(x, x')$, which are expressed as:

$$m(x) = E[f(x)] \quad (14)$$

$$k(x, x') = E\{[f(x) - m(x)][f(x') - m(x')]^T\} \quad (15)$$

where $f(x)$ is the target output, and x is the n-dimensional input vector. The corresponding Gaussian process expression is expressed as:

$$f(x) \sim GP[m(x), k(x, x')] \quad (16)$$

Generally, functions are noisy, assuming that the noise is additive, independent and Gaussian, so the relationship between input x and output y is:

$$y = f(x) + \varepsilon \quad (17)$$

where $\varepsilon \sim N(0, \sigma^2)$ is the white noise with variance σ_n^2 . The prior distribution of observed values can be expressed as:

$$y \sim N[0, K_f(x, x) + \sigma_n^2 I_n] \quad (18)$$

where I_n is the n-dimensional identity matrix. In the covariance matrix, hyperparameter $\theta = [\sigma_f, I, \sigma_n]$ can be optimized by maximizing likelihood, which is expressed as:

$$L = -\frac{1}{2} \log[\det[K_f(x, x) + \sigma_n^2 I_n]] - \frac{1}{2} y^T [K_f(x, x) + \sigma_n^2 I_n]^{-1} y - \frac{n}{2} \log 2\pi \quad (19)$$

The joint prior distribution of observed value y and predicted value y^* in the test dataset x^* is:

$$\begin{bmatrix} y \\ y^* \end{bmatrix} \sim N(0, \begin{bmatrix} K_f(x, x) + \sigma_n^2 & K_f(x, x^*) \\ K_f(x, x^*)^T & K_f(x^*, x^*) \end{bmatrix}) \quad (20)$$

Based on the joint prior distribution of y , the posterior distribution $p(y^*|x, y, y^*)$ can be calculated as:

$$p(y^*|x, y, y^*) = N[y^*|\bar{y}^*, \text{cov}(\bar{y}^*)] \quad (21)$$

In (21), predicting the average value \bar{y}^* and covariance $\text{cov}(\bar{y}^*)$ is as follows:

$$\bar{y}^* = K_f(x, x^*)^T [K_f(x, x) + \sigma_n^2 I_n]^{-1} y \quad (22)$$

$$\text{cov}(\bar{y}^*) = K_f(x^*, x^*) - K_f(x, x^*)^T \times [K_f(x, x) + \sigma_n^2 I_n]^{-1} K_f(x, x^*) \quad (23)$$

In [101], the largest international database on the impedance and corresponding aging of LIBs is established. Unlike previous studies, ARD is used to extract data from EIS data at frequencies (17.8 Hz and 2.16 Hz) that are highly correlated with SOH trends as input features. These are then combined with GPR for estimation. In addition, by combining the training data collected at three different temperatures (25°C, 35°C, and 45°C), the model can still achieve estimation at different temperatures. Experiments have been conducted on all charging and discharging states, and it is found that the fifth state is the optimal state for estimating the SOH. Compared with using discharge curve features as inputs to GPR, it is demonstrated that the EIS method achieves lower estimation errors (see Table 3).

It should be noted that the battery SOH is affected by the selected frequency, temperature, and the SOC. The selection of impedance data for a specific frequency cannot guarantee the accuracy of SOH estimation in a

dynamic environment [102]. The same dataset is used in [103] through unsupervised learning (InfoGAN), and features are extracted from full-frequency impedance data. Automatic feature extraction can be achieved through InfoGAN, which greatly reduces the time required. The extracted features are then applied to GPR to estimate the discharge capacity of the battery. The experimental results demonstrate that under all operating conditions of LIBs with a nominal capacity of 45 mAh, the fifth state has the best performance, and the estimation error is shown in Table 4.

4.3.2 Artificial neural network

Among the methods of machine learning, artificial neural networks (ANN) are the most prominent, with their strong robustness, fault tolerance, and generalizability [104]. ANN have become the center of deep learning and are now being used for tasks such as image classification, object detection, and cooling system design [105–107]. In addition, ANN can give full play to the high-speed computing ability of the computer, quickly find the optimal solution, and improve computing efficiency [108]. It is particularly advantageous to use neural networks for SOH estimation of LIBs, because the degradation mode of batteries can be learned by analyzing the impedance behavior of multiple batteries [109].

4.3.2.1 BP neural network Compared to model-based methods, data-driven methods do not require an understanding of the internal decay mechanism of LIBs. Only the measured data related to capacity decline need to be fed into the neural network, and the estimation of SOH can be realized by adjusting the hyperparameter of the network [110].

Reference [111] uses convolutional neural networks (CNN) to mine EIS data, and then estimates the cyclic lifespan of LIBs using fully connected neural networks (FNN). As shown in Fig. 9, the FNN configured in the experiment is a four-layer neural network. As a rule of thumb, the selection of the number of neurons in the hidden layer is determined by the number of neurons in the input layer. The estimated results are shown in Fig. 10. However, this method cannot be applied to online

Table 3 RMSE of EIS based method and method using discharge curve as input

Input	Cells			
	25C05	25C06	25C07	25C08
EIS	8.57	18.19	5.25	5.03
Capacity and voltage curves	43.22	34.28	38.14	73.20

Table 4 Estimation results of the fifth state data using EISGAN

Method	Stage	Cell	MAE (mAh)	RMSE (mAh)	R ²
EISGAN	5	25C05	0.7256	0.8569	0.8326
		25C06	0.7127	0.9114	0.7907
		25C07	1.6835	1.8063	0.0729
		25C08	1.7357	1.8676	0.3970

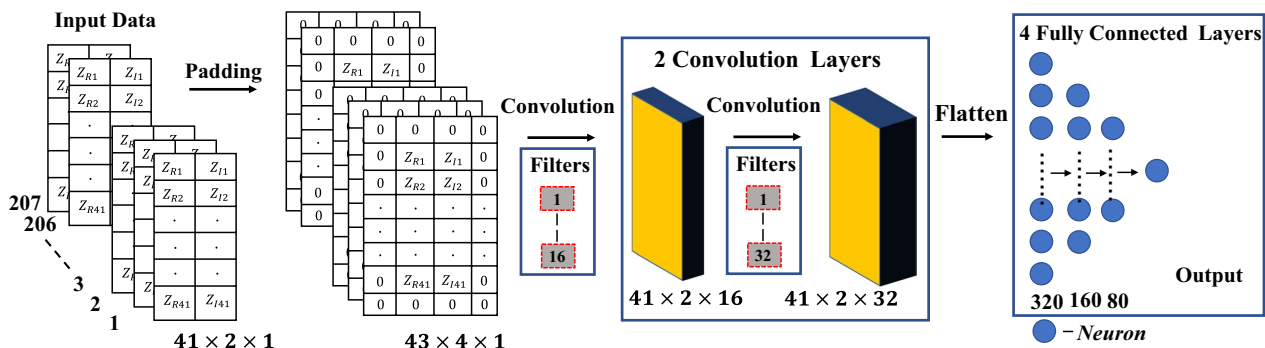


Fig. 9 Architecture of CNN estimation model. Reprinted with permission from [111]. Copyright 2022, Springer

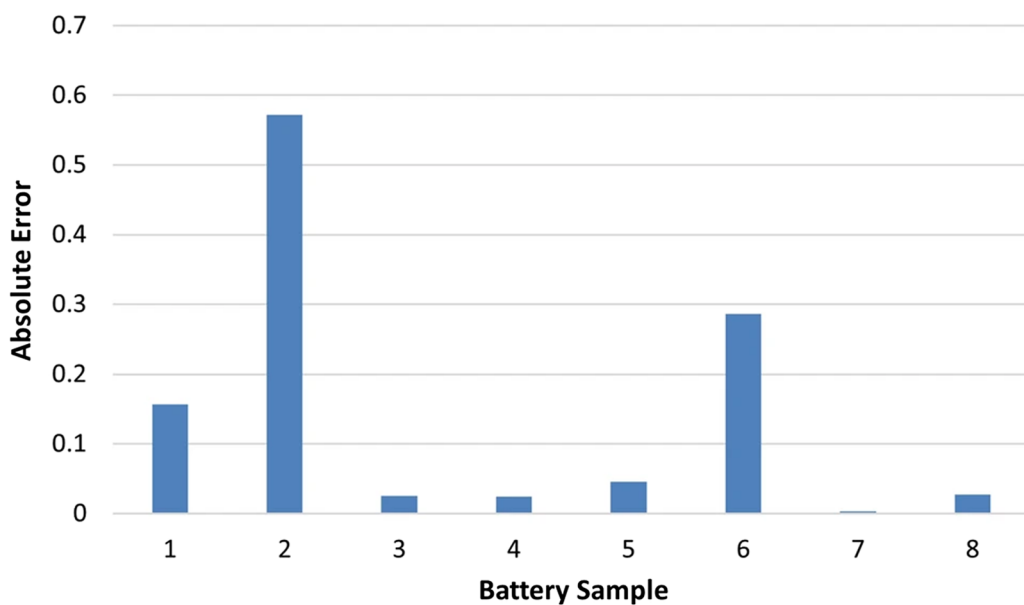


Fig. 10 Absolute error values for each of the samples

measurement, and the proposed model can only achieve estimation under 100% SOC conditions.

The backpropagation (BP) neural network introduces the backpropagation algorithm on the basis of FNN, and is mainly divided into two stages: forward propagation of signals and back propagation of errors. It sequentially adjusts the weight and bias from the hidden layer to the output layer, as well as the weight and bias from the input layer to the hidden layer. EIS data with frequencies ranging from 0.02 to 20 kHz are used in [112], and the preprocessed data are features learned through a convolutional autoencoder (CAE). Subsequently, a BP neural network consisting of four hidden layers and four dropout layers is used, and the input of this network is a flat potential feature extracted by the CAE. Applying L2 regularization with 0.001 L2 parameter, the specific process is shown in Fig. 11. Compared

to [103], the established model shows better predictive performance at 35°C and 45°C, with RMSEs of 0.0129 and 0.0112, respectively.

After verification, the correlation between ANN input and SOH determines the final evaluation. ANN does not need to delve into the internal operating mechanism of LIBs, and can better evaluate the aging trend of LIBs using previous information.

4.3.2.2 Extreme learning machine The Extreme learning machine (ELM) and BP are both based on the architecture of a feedforward neural network, and their differences lie in the different learning methods. The BP algorithm uses the gradient descent method to learn by using the back propagation method, and needs to update the weight and threshold constantly through iteration. In contrast, ELM learns by increasing the number of hidden layer nodes,

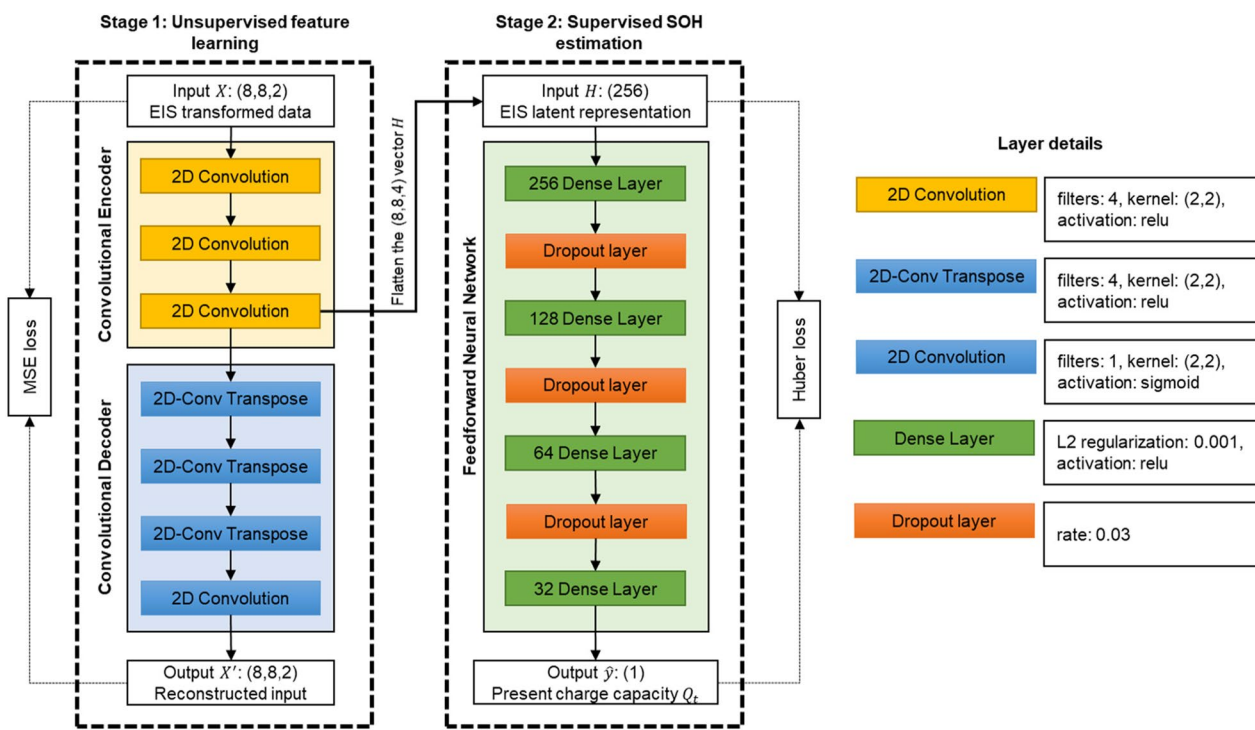


Fig. 11 Two-stage deep learning architecture for the proposed charge capacity prediction. Reprinted with permission from [112]. Copyright 2023, Springer

which are generally determined according to the number of samples, and linking the number of hidden layers with the number of samples. In many feedforward neural networks, the default maximum number of hidden layer nodes is the number of samples. It does not require iteration, so it is much faster than BP.

In [113], the Fast Fourier Transform (FFT) measurement of EIS is improved and a SOH estimation model is established in conjunction with ELM, as shown in Fig. 12. To ignore the impact of SOC, six EIS features that do not change with SOC but are closely related to SOH are selected as inputs within a specific frequency range. The Spearman correlation coefficient is used to test the correlation between HFs and aging ability. The results show that their RMSEs are all lower than 0.02.

4.3.2.3 Recurrent neural network Due to the lack of memory for previous weights and thresholds in full FNN, the estimation performance may be unstable. Although the use of a BP algorithm can optimize neural networks and converge weights to a certain value, it is easy for it to fall into local optima while not guaranteeing global optima.

The emergence of Recurrent Neural Networks (RNN) has effectively addressed these shortcomings. RNN consists of Simple-RNN, Long-Short-Term-Memory

(LSTM), and Gated-Recurrent-Unit (GRU). Because the gradient of a Simple-RNN disappears, RNN can only have short-term memory and cannot support the memory of a constant sequence. LSTM is a variant of RNN, which combines short- and long-term memory through sophisticated gate control, and solves the problem of gradient disappearance to some extent. As a variant of LSTM, GRU has a simpler structure than LSTM. When the dataset is small, it can achieve results comparable to LSTM and has higher estimation efficiency. Therefore, applying RNN to SOH of LIBs can produce more accurate estimation results.

The structure of LSTM is shown in Fig. 13. LSTM has three gates: the forgetting gate which discards excess information, the input gate which selects key information to be stored in the internal state, and the output gate which is used to determine the output information. Therefore, LSTM neural networks can effectively store and update key information over a long period of time without gradient vanishing [114].

The data processing process of an LSTM neural network is as follows:

Discard unnecessary information from the previous unit c_{t-1} in the forgetting gate f_t :

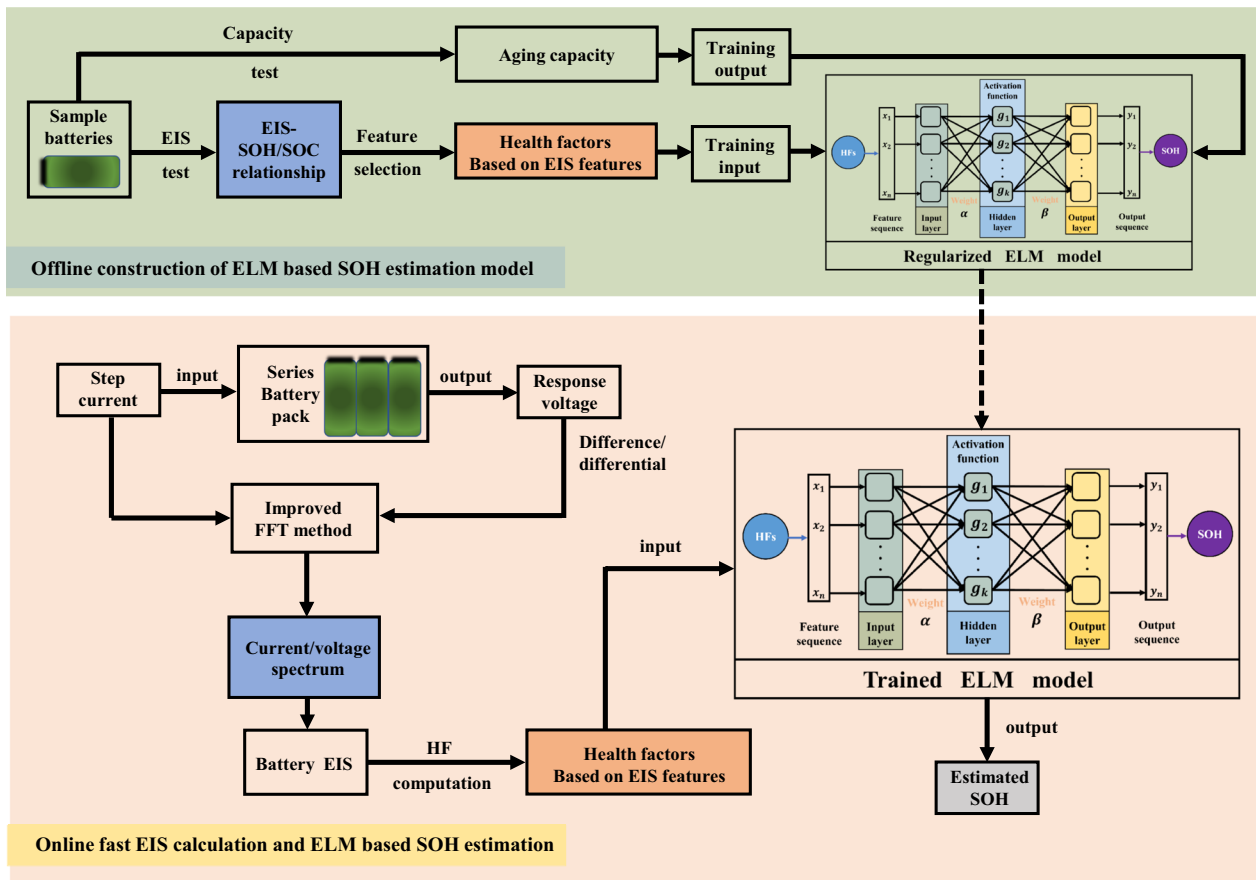


Fig. 12 Offline construction of ELM based SOH estimation model and online fast EIS calculation and ELM based SOH estimation block diagram. Reprinted with permission from [113]. Copyright 2022, IEEE

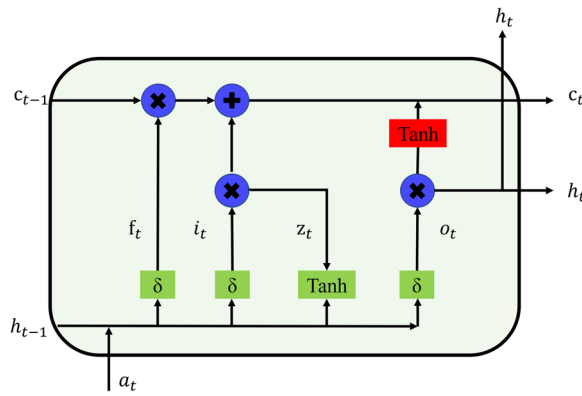


Fig. 13 The structure of LSTM

$$f_t = \sigma(w_f x_t + u_f h_{t-1} + b_f) \quad (24)$$

Update input units i_t and \tilde{c}_t :

$$i_t = \sigma(w_i x_t + u_i h_{t-1} + b_i) \quad (25)$$

$$\tilde{c}_t = \tanh(w_i x_t + u_i h_{t-1} + b_c) \quad (26)$$

Update unit C:

$$c_t = f_t c_{t-1} + i_t \tilde{c}_t \quad (27)$$

Generate output h_t based on input o_t and c_t :

$$o_t = \sigma(w_o x_t + u_o h_{t-1} + b_o) \quad (28)$$

Reference [115] uses the features extracted from EIS data using CNN as the input of the neural network, and the SOH of LIBs as the output. The initial value of the learning rate is set to 0.001, and the hidden layer is set to 56 units. A dropout algorithm is used to suppress overfitting, which is set to 0.5, and an Adam algorithm is used to optimize the neural network. An improved optimization algorithm is introduced to achieve

Table 5 The RMSE of different models for LIBs

Method	25C01	25C02	35C01	35C02	45C01	45C02
IPSO-CNN-BiLSTM	0.0176	0.0238	0.0145	0.0183	0.0236	0.0188
IPSO-CNN-BiLSTM	0.02	0.0268	0.0178	0.0238	0.0292	0.0216
CNN-BiLSTM	0.0341	0.0286	0.0209	0.0266	0.0385	0.0223
LSTM	0.0343	0.0368	0.0225	0.0281	0.0436	0.0239

Table 6 Comparison of SOH estimation methods based on EIS

Method	Advantages	Disadvantages
ECM	The model is simple, and can reflect the aging mechanism of the battery	Parameter identification error is large, poor generalization, and low model update rate
Data-driven	Easy to use, and no need to analyze the aging mechanism of the battery	Need a lot of data, and high calculation cost

automatic optimization of network parameters, and the final results are shown in Table 5. This demonstrates the importance of optimization algorithms for estimation performance.

Table 6 summarizes the two existing methods. The advantage of the ECM model is that the model structure is relatively simple, while the disadvantage is that the error in model parameter identification will continue to increase. Additionally, the estimation accuracy is greatly affected by the ECM structure. In terms of adaptability, ECM-based methods are generally used for laboratory research. The data-driven approach is based on collecting data and mining hidden information through various data analysis and machine learning methods for estimation. However, this method has a serious dependence on data, and the obtained data may have uncertainty and incompleteness. It is also unrealistic to test all possible life influencing factors in practical applications. Although this estimation method is easy to implement, it is not widely used at present because of the current level of hardware and data storage technology.

5 Summary and prospects

The precise estimation of the SOH in LIBs is beneficial for the development of various fields such as battery production, cascade utilization, and recycling. At present, the testing of EIS mostly relies on expensive electrochemical workstations, so they are mostly used for laboratory research on batteries. The SOH estimation methods of LIBs can be roughly divided into fitting model-based and data-driven methods, each with its own advantages and disadvantages. In recent years, data-driven methods have become a research hotspot. However, this method requires a large amount of comprehensive data to establish the model, and because of the presence of noise

pollution, the accuracy of the data will directly affect the quality of the evaluation results. Therefore, ensuring high-precision data collection is a key technical issue that needs to be overcome. In addition, under the same estimation model, the setting of the initial value of the model and the selection of hyperparameter will affect the evaluation results. It is necessary to extract highly correlated features from EIS data, and consequently it is necessary to develop a new type of sequence estimation model to improve evaluation accuracy.

In reality, batteries are usually connected in series and/or parallel to form a battery pack. Under normal operating conditions, there are inherently different changes between the batteries in the battery pack, and as the batteries age, the changes between the batteries will become greater. This will result in SOH deviation between individual batteries in the battery pack. Therefore, the SOH estimation method for a single battery may not be applicable to battery packs. Although the above research has achieved certain milestones in individual batteries, adjusting SOH estimation technology from individual batteries to battery packs remains a huge challenge.

Abbreviations

LIBs	Lithium-ion batteries
SOH	State-of-health
BMS	Battery management system
EIS	Electrochemical impedance spectroscopy
ECM	Equivalent circuit model
FT	Fourier transform
FFT	Fast Fourier transformation
CNN	Convolution neural network
RMSE	Root mean square error
K-K	Kramers-Kronig
SEI	Solid electrolyte interface
SOC	State-of-charge
IOM	Integer order model
FOM	Fractional order model
CPE	Constant phase element

CNLS	Complex nonlinear least squares
FIM	Fractional impedance model
RUL	Remaining useful life
RLS	Recursive least squares
SVF	State variable filter
PF	Particle filter
GPR	Gaussian process regression
ELM	Extreme learning machine

Acknowledgements

This work was supported by the Youth Fund of Shandong Province Natural Science Foundation (No. ZR2020QE212), Key Projects of Shandong Province Natural Science Foundation (No. ZR2020KF020), the Guangdong Provincial Key Lab of Green Chemical Product Technology (GC202111), Zhejiang Province Natural Science Foundation (No. LY22E070007) and National Natural Science Foundation of China (No. 52007170).

Author contributions

Conceptualization, Y.L. and D.L.; methodology, D.L. and L.W.; investigation, K.W.; writing—original draft preparation, Y.L.; writing—review and editing, Y.L. and L.W.; All authors have read and agreed to the published version of the manuscript.

Funding

This work was supported by the Youth Fund of Shandong Province Natural Science Foundation (No. ZR2020QE212), Key Projects of Shandong Province Natural Science Foundation (No. ZR2020KF020), the Guangdong Provincial Key Lab of Green Chemical Product Technology (GC202111), Zhejiang Province Natural Science Foundation (No. LY22E070007) and National Natural Science Foundation of China (No. 52007170).

Availability of data and materials

The data and materials used to support the findings of this study are available from the corresponding author upon request.

Declarations

Competing interests

The authors declare that they have no known competing financial interests or personal relationships that could have appeared to influence the work reported in this paper.

Received: 22 February 2023 Accepted: 1 August 2023

Published online: 31 August 2023

References

- Harper, G., Sommerville, R., Kendrick, E., et al. (2019). Recycling lithium-ion batteries from electric vehicles. *Nature*, 575(7781), 75–86.
- Huixin, T., Pengliang, Q., Kun, L., et al. (2020). A review of the state of health for lithium-ion batteries: Research status and suggestions. *Journal of Cleaner Production*, 261, 120813.
- Yang, S., Zhang, C. P., Jiang, J. C., et al. (2021). Review on state-of-health of lithium-ion batteries: Characterizations, estimations and applications. *Journal of Cleaner Production*, 314, 128015.
- Liu, C., Li, D., Wang, L., et al. (2022). Strong robustness and high accuracy in predicting remaining useful life of supercapacitors. *APL Materials*, 10(6), 061106.
- Zeng, X., Li, M., Abd El-Hady, D., et al. (2019). Commercialization of lithium battery technologies for electric vehicles. *Advanced Energy Materials*, 9(27), 1900161.
- Wang, L., Xie, L., Yang, Y., et al. (2023). Distributed online voltage control with fast PV power fluctuations and imperfect communication. *IEEE Transactions on Smart Grid*. 2023:1–14.
- Ma, N., Yang, D., Riaz, S., et al. (2023). Aging mechanism and models of supercapacitors: A review. *Technologies*, 11(2), 38.
- Zhang, M., Wang, W., Xia, G., et al. (2023). Self-powered electronic skin for remote human-machine synchronization. *ACS Applied Electronic Materials*, 5(1), 498–508.
- Yu, X., Li, Y., Li, X., et al. (2023). Research on outdoor mobile music speaker battery management algorithm based on dynamic redundancy. *Technologies*, 11(2), 60.
- Ma, N., Yin, H., & Wang, K. (2023). Prediction of the remaining useful life of supercapacitors at different temperatures based on improved long short-term memory. *Energies*, 16(14), 5240.
- Xin, S., Zhang, X., Ding, F., et al. (2021). Advanced electrode materials in lithium batteries: Retrospect and prospect. *Energy Material Advances*, 2021, 1–15.
- Xia, Q., Li, X., Wang, K., et al. (2022). Unraveling the evolution of transition metals during Li alloying-dealloying by in-operando magnetometry. *Chemistry of Materials*, 34(13), 5852–5859.
- Ge, M., Liu, Y., Jiang, X., et al. (2021). A review on state of health estimations and remaining useful life prognostics of lithium-ion batteries. *Measurement*, 174, 109057.
- Scrosati, B., & Garche, J. (2010). Lithium batteries: Status, prospects and future. *Journal of Power Sources*, 195(9), 2419–2430.
- Cui, Z., Kang, L., Li, L., et al. (2022). A hybrid neural network model with improved input for state of charge estimation of lithium-ion battery at low temperatures. *Renewable Energy*, 198, 1328–1340.
- Guo, Y., Yu, P., Zhu, C., et al. (2022). A state-of-health estimation method considering capacity recovery of lithium batteries. *International Journal of Energy Research*, 46(15), 23730–23745.
- Zhang, M., Wang, K., & Zhou, Y. (2020). Online state of charge estimation of lithium-ion cells using particle filter-based hybrid filtering approach. *Complexity*, 2020, 1–10.
- Yu, X., Ma, N., Zheng, L., et al. (2023). Developments and applications of artificial intelligence in music education. *Technologies*, 11(2), 42.
- Z. Yi, Z. Chen, K. Yin et al. Sensing as the key to the safety and sustainability of new energy storage devices. Protection and Control of Modern Power Systems. 2023,8(1):<https://doi.org/10.1186/s41601-41023-00300-41602>.
- Wang, N., Garg, A., Su, S., et al. (2022). Echelon utilization of retired power lithium-ion batteries: Challenges and prospects. *Batteries*, 8(8), 96.
- Weng, C., Cui, X., Sun, H., et al. (2013). On-board state of health monitoring of lithium-ion batteries using incremental capacity analysis with support vector regression. *Journal of Power Sources*, 235, 36–44.
- Weng, C., Feng, G., Sun, J., et al. (2016). State-of-health monitoring of lithium-ion battery modules and packs via incremental capacity peak tracking. *Applied Energy*, 180, 360–368.
- Berecibar, M., Garmendia, M., Gandiaga, I., et al. (2016). State of health estimation algorithm of LiFePO₄ battery packs based on differential voltage curves for battery management system application. *Energy*, 103, 784–796.
- Berecibar, M., Devriendt, F., Dubarry, M., et al. (2016). Online state of health estimation on NMC cells based on predictive analytics. *Journal of Power Sources*, 320, 239–250.
- Richardson, R. R., Birk, C. R., Osborne, M. A., et al. (2019). Gaussian process regression for in situ capacity estimation of lithium-ion batteries. *IEEE Transactions on Industrial Informatics*, 15(1), 127–138.
- Severson, K. A., Attia, P. M., Jin, N., et al. (2019). Data-driven prediction of battery cycle life before capacity degradation. *Nature Energy*, 4(5), 383–391.
- Pastor-Fernández, C., Uddin, K., Chouchelamane, G. H., et al. (2017). A comparison between electrochemical impedance spectroscopy and incremental capacity-differential voltage as li-ion diagnostic techniques to identify and quantify the effects of degradation modes within battery management systems. *Journal of Power Sources*, 360, 301–318.
- Kazda, T., Gavalierova, V., Dostal, P., et al. (2021). Detection of the Changes in Li-ion Batteries Using Nondestructive Methods. *ECS Transactions*, 105, 21–28.
- Zhang, M., Liu, Y., Li, D., et al. (2023). electrochemical impedance spectroscopy: A new chapter in the fast and accurate estimation of the state of health for lithium-ion batteries. *Energies*, 16(4), 1599.
- M. Zhang, D. Yang, J. Du et al. A Review of SOH Prediction of Li-Ion Batteries Based on Data-Driven Algorithms. *Energies*. 2023,16(7).

31. Cui, Z., Kang, L., Li, L., et al. (2022). A combined state-of-charge estimation method for lithium-ion battery using an improved GRU network and UKF. *Energy*, 259, 124933.
32. Guo, Y., Yang, D., Zhang, Y., et al. (2022). Online estimation of SOH for lithium-ion battery based on SSA-Elman neural network. *Protection and Control of Modern Power Systems*, 7(1), 40.
33. Choi, W., Shin, H., Kim, J. M., et al. (2020). Modeling and applications of electrochemical impedance spectroscopy (EIS) for lithium-ion batteries. *Journal of Electrochemical Science and Technology*, 11(1), 1–13.
34. Schuster, S. F., Brand, M. J., Campestrini, C., et al. (2016). Correlation between capacity and impedance of lithium-ion cells during calendar and cycle life. *Journal of Power Sources*, 305, 191–199.
35. Huet, F. (1998). A review of impedance measurements for determination of the state-of-charge or state-of-health of secondary batteries. *Journal of Power Sources*, 70(1), 59–69.
36. Galeotti, M., Cinà, L., Giannanco, C., et al. (2015). Performance analysis and SOH (state of health) evaluation of lithium polymer batteries through electrochemical impedance spectroscopy. *Energy*, 89, 678–686.
37. Zhou, X., Pan, Z., Han, X., et al. (2019). An easy-to-implement multi-point impedance technique for monitoring aging of lithium ion batteries. *Journal of Power Sources*, 417, 188–192.
38. Huang, W., & Qahouq, J. A. A. (2014). An online battery impedance measurement method using DC–DC power converter control. *IEEE Transactions on Industrial Electronics*, 61(11), 5987–5995.
39. Din, E., Schaeff, C., Moffat, K., et al. (2017). A scalable active battery management system with embedded real-time electrochemical impedance spectroscopy. *IEEE Transactions on Power Electronics*, 32(7), 5688–5698.
40. Varnosfaderani, M. A., & Strickland, D. (2016). Online impedance spectroscopy estimation of a battery. In *2016 18th European conference on power electronics and applications (EPE'16 ECCE Europe)*. 2016:1–10.
41. Xia, Z., & Qahouq, J. A. A. (2017). Method for online battery AC impedance spectrum measurement using dc–dc power converter duty-cycle control. *IEEE Applied Power Electronics Conference and Exposition (APEC)*, 2017, 1999–2003.
42. Hampson, N. A., & Karunathilaka, S. A. G. R. (1980). The impedance of electrical storage cells. *Journal of Applied Electrochemistry*, 10, 3–11.
43. Křivík, P., Vaculík, S., Bača, P., et al. (2019). Determination of state of charge of lead-acid battery by EIS. *Journal of Energy Storage*, 21, 581–585.
44. Huang, J., Li, Z., Liaw, B. Y., et al. (2016). Graphical analysis of electrochemical impedance spectroscopy data in Bode and Nyquist representations. *Journal of Power Sources*, 309, 82–98.
45. Lindahl, P. A., Cornachione, M. A., & Shaw, S. R. (2012). A time-domain least squares approach to electrochemical impedance spectroscopy. *IEEE Transactions on Instrumentation and Measurement*, 61(12), 3303–3311.
46. Deleebeeck, L., & Veltzé, S. (2020). Electrochemical impedance spectroscopy study of commercial Li-ion phosphate batteries: A metrology perspective. *International Journal of Energy Research*, 44(9), 7158–7182.
47. Arora, S., Shen, W., & Kapoor, A. (2016). Review of mechanical design and strategic placement technique of a robust battery pack for electric vehicles. *Renewable and Sustainable Energy Reviews*, 60, 1319–1331.
48. Katayama, N., & Kogoshi, S. (2013). Mixed-signal fourier transform for electrochemical impedance spectroscopy. *Journal of Fuel Cell Science and Technology*, 10(1), 011006.
49. Lu, P., Li, M., Zhang, L., et al. (2019). A novel Fast-EIS measuring method and implementation for lithium-ion batteries. *Prognostics and System Health Management Conference*, 2019, 1–6.
50. Gomez-Luna, E., Silva, D., Aponte, G., et al. (2013). Obtaining the electrical impedance using wavelet transform from the time response. *IEEE Transactions on Power Delivery*, 28(2), 1242–1244.
51. Debenjak, A., Boškoski, P., Musizza, B., et al. (2014). Fast measurement of proton exchange membrane fuel cell impedance based on pseudo-random binary sequence perturbation signals and continuous wavelet transform. *Journal of Power Sources*, 254, 112–118.
52. Boukamp, B. A. (1995). A linear Kronig-Kramers transform test for impedance data validation. *Journal of the Electrochemical Society*, 142(6), 1885–1894.
53. Sun, H., Sun, J., Zhao, K., et al. (2022). Data-driven ICA-Bi-LSTM-combined lithium battery SOH estimation. *Mathematical Problems in Engineering*, 2022, 1–8.
54. Mertens, A., Vinke, I. C., Tempel, H., et al. (2016). Quantitative analysis of time-domain supported electrochemical impedance spectroscopy data of li-ion batteries: Reliable activation energy determination at low frequencies. *Journal of the Electrochemical Society*, 163(7), H521–H527.
55. Erol, S., Orazem, M. E., & Muller, R. P. (2014). Influence of overcharge and over-discharge on the impedance response of $\text{LiCoO}_2|\text{C}$ batteries. *Journal of Power Sources*, 270, 92–100.
56. Aurbach, D., Markovsky, B., Weissman, I., et al. (1999). On the correlation between surface chemistry and performance of graphite negative electrodes for Li ion batteries. *Electrochimica Acta*, 45(1–2), 67–86.
57. Jung, S., Gwon, H., Hong, J., et al. (2014). Understanding the degradation mechanisms of $\text{LiNi}_{0.5}\text{Co}_{0.2}\text{Mn}_{0.3}\text{O}_2$ cathode material in lithium ion batteries. *Advanced Energy Materials*, 4(1), 1300787.
58. Novák, P., Joho, F., Lanz, M., et al. (2001). The complex electrochemistry of graphite electrodes in lithium-ion batteries. *Journal of Power Sources*, 97–98, 39–46.
59. Verma, P., Maire, P., & Novák, P. (2010). A review of the features and analyses of the solid electrolyte interphase in Li-ion batteries. *Electrochimica Acta*, 55(22), 6332–6341.
60. Witt, D., Röder, F., & Kreuer, U. (2022). Analysis of lithium-ion battery state and degradation via physicochemical cell and SEI modeling. *Batteries & Supercaps*, 5(7), e202200067.
61. Xu, H., Han, C., Li, W., et al. (2022). Quantification of lithium dendrite and solid electrolyte interphase (SEI) in lithium-ion batteries. *Journal of Power Sources*, 529, 231219.
62. Birk, C. R., Roberts, M. R., McTurk, E., et al. (2017). Degradation diagnostics for lithium ion cells. *Journal of Power Sources*, 341, 373–386.
63. Pop, V., Bergveld, H. J., Regtien, P. P. L., et al. (2007). Battery aging and its influence on the electromotive force. *Journal of the Electrochemical Society*, 154(8), A744–A750.
64. Dubarry, M., Truchot, C., & Liaw, B. Y. (2012). Synthesize battery degradation modes via a diagnostic and prognostic model. *Journal of Power Sources*, 219, 204–216.
65. Yoshida, T., Takahashi, M., Morikawa, S., et al. (2006). Degradation mechanism and life prediction of lithium-ion batteries. *Journal of the Electrochemical Society*, 153(3), A576.
66. Petzl, M., Kasper, M., & Danzer, M. A. (2015). Lithium plating in a commercial lithium-ion battery – A low-temperature aging study. *Journal of Power Sources*, 275, 799–807.
67. Schindler, S., & Danzer, M. A. (2017). A novel mechanistic modeling framework for analysis of electrode balancing and degradation modes in commercial lithium-ion cells. *Journal of Power Sources*, 343, 226–236.
68. Stiaszny, B., Ziegler, J. C., Krauß, E. E., et al. (2014). Electrochemical characterization and post-mortem analysis of aged $\text{LiMn}_{2}\text{O}_4$ –NMC/graphite lithium ion batteries part II: Calendar aging. *Journal of Power Sources*, 258, 61–75.
69. de Vries, H., Nguyen, T. T., & het Veld, B. O. (2015). Increasing the cycle life of lithium ion cells by partial state of charge cycling. *Microelectronics Reliability*, 55(11), 2247–2253.
70. Lyu, C., Zhang, T., Luo, W., et al. (2019). SOH estimation of lithium-ion batteries based on fast time domain impedance spectroscopy. In *2019 14th IEEE conference on industrial electronics and applications (ICIEA)* (pp. 2142–2147).
71. Wong, D., Shrestha, B., Wetz, D. A., et al. (2015). Impact of high rate discharge on the aging of lithium nickel cobalt aluminum oxide batteries. *Journal of Power Sources*, 280, 363–372.
72. Shafiei Sabet, P., Warnecke, A. J., Meier, F., et al. (2020). Non-invasive yet separate investigation of anode/cathode degradation of lithium-ion batteries (nickel-cobalt-manganese vs. graphite) due to accelerated aging. *Journal of Power Sources*, 449, 227369.
73. Zhang, Y., & Wang, C. (2009). Cycle-life characterization of automotive lithium-ion batteries with LiNiO_2 cathode. *Journal of the Electrochemical Society*, 156(7), A527.
74. Li, J., Zhang, J., Zhang, X., et al. (2010). Study of the storage performance of a Li-ion cell at elevated temperature. *Electrochimica Acta*, 55(3), 927–934.

75. Westerhoff, U., Kurbach, K., Lienesch, F., et al. (2016). Analysis of lithium-ion battery models based on electrochemical impedance spectroscopy. *Energy Technology*, 4(12), 1620–1630.
76. Pulido, Y. F., Blanco, C., Anseán, D., García, V. M., Ferrero, F., & Valledor, M. (2017). Determination of suitable parameters for battery analysis by electrochemical impedance spectroscopy. *Measurement*, 106, 1–11.
77. Freeborn, T. J., Maundy, B., & Elwakil, A. S. (2015). Fractional-order models of supercapacitors, batteries and fuel cells: A survey. *Materials for Renewable and Sustainable Energy*, 4(3), 9.
78. Guha, A., & Patra, A. (2018). Online estimation of the electrochemical impedance spectrum and remaining useful life of lithium-ion batteries. *IEEE Transactions on Instrumentation and Measurement*, 67(8), 1836–1849.
79. Huang, Q., Shen, Y., Huang, Y., et al. (2016). Impedance characteristics and diagnoses of automotive lithium-ion batteries at 7.5% to 93.0% state of charge. *Electrochimica Acta*, 219, 751–765.
80. Murbach, M., Gerwe, B., Dawson-Elli, N., et al. (2020). impedance p.y.: A Python package for electrochemical impedance analysis. *Journal of Open Source Software*, 5(52), 2349.
81. Vyroubal, P., & Kazda, T. (2018). Equivalent circuit model parameters extraction for lithium ion batteries using electrochemical impedance spectroscopy. *Journal of Energy Storage*, 15, 23–31.
82. Plett, G. L. (2011). Recursive approximate weighted total least squares estimation of battery cell total capacity. *Journal of Power Sources*, 196(4), 2319–2331.
83. Mc Carthy, K., Gullapalli, H., Ryan, K. M., et al. (2021). Review-use of impedance spectroscopy for the estimation of li-ion battery state of charge, state of health and internal temperature. *Journal of the Electrochemical Society*, 168(8), 080517.
84. Zhang, X., Zhang, W., & Lei, G. (2016). A review of li-ion battery equivalent circuit models. *Transactions on Electrical and Electronic Materials*, 17(6), 311–316.
85. Iurilli, P., Brivio, C., & Wood, V. (2021). On the use of electrochemical impedance spectroscopy to characterize and model the aging phenomena of lithium-ion batteries: A critical review. *Journal of Power Sources*, 505, 229860.
86. Hammouche, A., Karden, E., & De Doncker, R. W. (2004). Monitoring state-of-charge of Ni-MH and Ni-Cd batteries using impedance spectroscopy. *Journal of Power Sources*, 127(1–2), 105–111.
87. Andre, D., Meiler, M., Steiner, K., et al. (2011). Characterization of high-power lithium-ion batteries by electrochemical impedance spectroscopy. I. Experimental investigation. *Journal of Power Sources*, 196(12), 5334–5341.
88. Li, Y., Dong, B., Zerrin, T., et al. (2020). State-of-health prediction for lithium-ion batteries via electrochemical impedance spectroscopy and artificial neural networks. *Energy Storage*, 2(5), e186.
89. Xiao, R., Shen, J., Li, X., et al. (2016). Comparisons of modeling and state of charge estimation for lithium-ion battery based on fractional order and integral order methods. *Energies*, 9(3), 184.
90. Alavi, S. M. M., Birk, C. R., & Howey, D. A. (2015). Time-domain fitting of battery electrochemical impedance models. *Journal of Power Sources*, 288, 345–352.
91. Zhang, Q., Huang, C., Li, H., et al. (2022). Electrochemical Impedance Spectroscopy based state of health estimation for lithium-ion battery considering temperature and state of charge effect. *IEEE Transactions on Transportation Electrification*, 8(4), 1–14.
92. Xiong, R., Tian, J., Mu, H., et al. (2017). A systematic model-based degradation behavior recognition and health monitoring method for lithium-ion batteries. *Applied Energy*, 207, 372–383.
93. Stroe, D. I., Swierczynski, M., Stan, A. I., et al. (2014). Diagnosis of lithium-ion batteries state-of-health based on electrochemical impedance spectroscopy technique. *IEEE Energy Conversion Congress and Exposition*, 2014, 4576–4582.
94. Wang, X., Wei, X., & Dai, H. (2019). Estimation of state of health of lithium-ion batteries based on charge transfer resistance considering different temperature and state of charge. *Journal of Energy Storage*, 21, 618–631.
95. Mu, H., Xiong, R., Zheng, H., et al. (2017). A novel fractional order model based state-of-charge estimation method for lithium-ion battery. *Applied Energy*, 207, 384–393.
96. Yang, Q., Xu, J., Li, X., et al. (2020). State-of-health estimation of lithium-ion battery based on fractional impedance model and interval capacity. *International Journal of Electrical Power & Energy Systems*, 119, 105883.
97. Jiang, B., Zhu, J., Wang, X., et al. (2022). A comparative study of different features extracted from electrochemical impedance spectroscopy in state of health estimation for lithium-ion batteries. *Applied Energy*, 322, 119502.
98. Liu, C., Zhang, Y., Sun, J., et al. (2021). Stacked bidirectional LSTM RNN to evaluate the remaining useful life of supercapacitor. *International Journal of Energy Research*, 46(3), 3034–3043.
99. Richardson, R. R., Osborne, M. A., & Howey, D. A. (2017). Gaussian process regression for forecasting battery state of health. *Journal of Power Sources*, 357, 209–219.
100. Yang, D., Zhang, X., Pan, R., et al. (2018). A novel Gaussian process regression model for state-of-health estimation of lithium-ion battery using charging curve. *Journal of Power Sources*, 384, 387–395.
101. Zhang, Y., Tang, Q., Zhang, Y., et al. (2020). Identifying degradation patterns of lithium ion batteries from impedance spectroscopy using machine learning. *Nature Communications*, 11(1), 1706.
102. Gordon, I. A. J., Gruegeon, S., Takenouti, H., et al. (2017). Electrochemical Impedance Spectroscopy response study of a commercial graphite-based negative electrode for Li-ion batteries as function of the cell state of charge and ageing. *Electrochimica Acta*, 223, 63–73.
103. Kim, S., Choi, Y. Y., & Choi, J.-I. (2022). Impedance-based capacity estimation for lithium-ion batteries using generative adversarial network. *Applied Energy*, 308, 118317.
104. Cui, Z., Wang, L., Li, Q., et al. (2021). A comprehensive review on the state of charge estimation for lithium-ion battery based on neural network. *International Journal of Energy Research*, 46(5), 5423–5440.
105. Mahmon, N. A., & Ya'acob, N. (2014). A review on classification of satellite image using artificial neural network (ANN). In *2014 IEEE 5th control and system graduate research colloquium* (pp. 153–157).
106. Yusri, I. M., Abdul Majeed, A. P. P., Mamat, R., et al. (2018). A review on the application of response surface method and artificial neural network in engine performance and exhaust emissions characteristics in alternative fuel. *Renewable and Sustainable Energy Reviews*, 90, 665–686.
107. Jani, D. B., Mishra, M., & Sahoo, P. K. (2017). Application of artificial neural network for predicting performance of solid desiccant cooling systems-A review. *Renewable and Sustainable Energy Reviews*, 80, 352–366.
108. Hussein, A. A. (2015). Capacity fade estimation in electric vehicle li-ion batteries using artificial neural networks. *IEEE Transactions on Industry Applications*, 51(3), 2321–2330.
109. Tummala, S., Bhagavatula, S. V., Yellamraju, V. R. B., et al. (2020). ANN based battery health monitoring - a comprehensive review. *E3S Web of Conferences*, 184, 01068.
110. Wang, S., Ren, P., Takyi-Aninakwa, P., et al. (2022). A critical review of improved deep convolutional neural network for multi-timescale state prediction of lithium-ion batteries. *Energies*, 15(14), 5053.
111. Pradyumna, T. K., Cho, K., Kim, M., et al. (2022). Capacity estimation of lithium-ion batteries using convolutional neural network and impedance spectra. *Journal of Power Electronics*, 22(5), 850–858.
112. Obregon, J., Han, Y., Ho, C. W., et al. (2023). Convolutional autoencoder-based SOH estimation of lithium-ion batteries using electrochemical impedance spectroscopy. *Journal of Energy Storage*, 60, 106680.
113. Fu, Y., Xu, J., Shi, M., et al. (2022). A fast impedance calculation-based battery state-of-health estimation method. *IEEE Transactions on Industrial Electronics*, 69(7), 7019–7028.
114. Wang, S., Takyi-Aninakwa, P., Jin, S., et al. (2022). An improved feedforward-long short-term memory modeling method for the whole-life-cycle state of charge prediction of lithium-ion batteries considering current-voltage-temperature variation. *Energy*, 254, 124224.
115. Li, D., Yang, D., Li, L., et al. (2022). Electrochemical impedance spectroscopy based on the state of health estimation for lithium-ion batteries. *Energies*, 15(18), 6665.